Editors' Suggestion | Featured in Physics

Stratification-Dependent Enstrophy-Controlled Regime in Geostrophic Turbulence

Shan-Shan Ding,[1,*] Hadrien Bobas,[2] Hélène Scolan,[3] Roland M. B. Young,[4] and Peter L. Read[1,†]

[1]Atmospheric, Oceanic and Planetary Physics, Department of Physics, University of Oxford, OX1 3PU, United Kingdom

[2]Université Paris-Saclay, ENS Paris-Saclay, DER de Physique, 91190, Gif-sur-Yvette, France

[3]Université Claude Bernard Lyon 1, Laboratoire de Mécanique des Fluides et d'Acoustique, UMR5509, CNRS, École Centrale de Lyon, INSA Lyon, 69622 Villeurbanne, France

[4]Department of Physics, SUPA, University of Aberdeen, King's College, Aberdeen, United Kingdom

(Received 19 November 2025; accepted 10 February 2026; published 20 March 2026)

We experimentally measure geostrophic turbulence in a rotating, differentially heated fluid annulus, which is bounded by convectively driven warm and cold flows at the outer and inner boundaries, respectively. The horizontal kinetic energy spectra exhibit a range at low wave number which scales as k^{-3}, where k denotes the horizontal wave number, with spectral amplitude that correlates with the square of the Brunt-Väisälä frequency at the same heights as the velocity measurements. The observed turbulent state exhibits a forward enstrophy cascade across all scales along with bidirectional energy transfer, which is evidenced by a reversal in the sign of the spectral energy flux at a scale proportional to the internal Rossby radius of deformation. These findings highlight the role of baroclinic instability in shaping the distribution of energy across scales, with implications for synoptic-scale turbulent flows near Earth's tropopause.

DOI: 10.1103/n2nj-dg5r

The distribution and transfer of energy in planetary turbulent flows, such as midlatitude zonal flow, tropical cyclones, polar vortices, etc., have long been subjects of fundamental interest. The flow structure may draw energy either from kinetic energy in the presence of shear flows via barotropic instability or from potential energy stored in stably stratified flows with inclined isothermal surfaces via baroclinic instability [1] given a source of potential energy produced by latitudinally inhomogeneous instellation. In the latter circumstance, the misalignment between potential temperature and pressure gradients can lead to the generation of baroclinic eddies with a characteristic length scale determined *inter alia* by the stratification strength. Baroclinic eddies play a crucial role in flow pattern selection, energetics, and vorticity dynamics for a range of natural systems, from the atmospheric and oceanic circulations on planets [2–5] to turbulence in accretion disks [6], as well as in engineering contexts such as in semiconductor crystal growth [7].

In the Earth's troposphere, the characteristic baroclinic length scale is on the order of 1000 km, much larger than the tropospheric thickness, leading to complex dynamics analogous in some respects to two-dimensional (2D) turbulence [8]. The Kraichnan-Leith-Batchelor (KLB) theory for 2D turbulence predicts a kinetic energy spectrum of the form $\eta^{2/3}k^{-3}$ for a downscale enstrophy transfer regime, where wave number k is typically greater than that corresponding to the energy injection [9,10]. The existence of this spectral slope near the tropopause was first identified in aircraft observations [11], and the associated downscale enstrophy cascade, characterized by a slowly varying (with wave number) enstrophy flux η, has been validated using observation data or global numerical simulations [12,13]. This spectral regime is marked by the dominance of the vortical component of the flow [14], suggesting an important role for baroclinic eddies in shaping the spectra. A natural question arises concerning how baroclinic eddies shape the energy spectrum at synoptic scales. An equivalent question is how baroclinic eddies link to the enstrophy flux. Although much effort has been devoted to understanding the process of producing the mesoscale spectra with a shallow spectral slope of $-5/3$, which is likely associated with the internal gravity waves emitted by the unbalanced motion of baroclinic flows [15], the relationship of the k^{-3} segment of the spectrum to baroclinic processes is less well understood. This steep spectral slope could also emerge from other scenarios, such as a self-similar hierarchy of vortices or a limited ensemble of vortices condensed to the domain size in two-dimensional turbulence or, in rotating Rayleigh-Bénard convection, in a situation where energy is being injected by a process at scales much smaller than the system size [16–18].

Experimental setup—To address the relevance of baroclinic instability to this question, we constructed a cylindrical annular laboratory model, as shown in Fig. 1(a), that emulated key aspects of the midlatitude atmospheric

*Contact author: shanshan.ding@physics.ox.ac.uk

†Contact author: peter.read@physics.ox.ac.uk

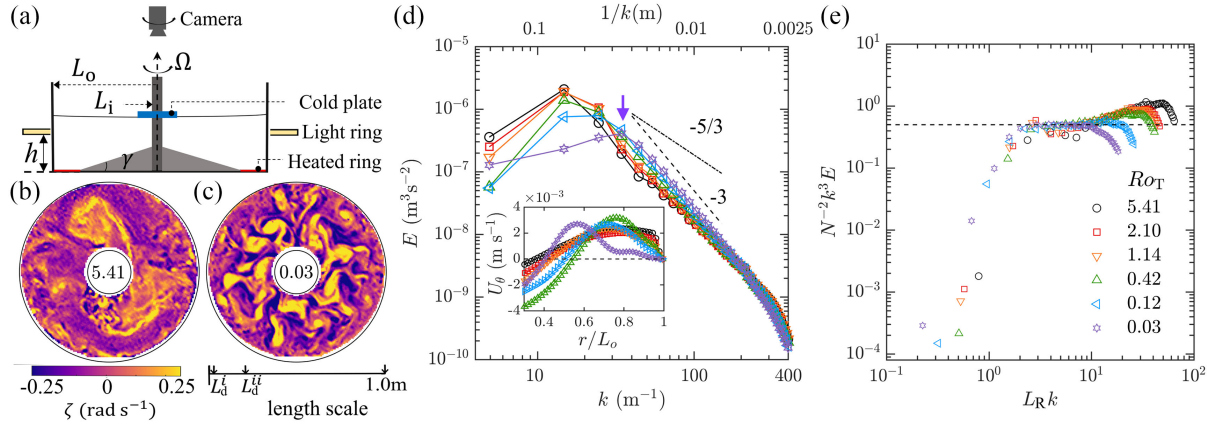

FIG. 1. (a) Schematic plot of the convective tank. Snapshots of ζ for $Ro_T = 5.41$ (b) and $Ro_T = 0.03$ (c). On the scale bar, $L_d^i = 2.4$ cm and $L_d^{ii} = 22.6$ cm are the Rossby radius of deformation for (c) and (b), respectively. (d) Kinetic energy spectra, $E(k)$, for various Ro_T. The arrow indicates the wave number k_p corresponding to the peak of $E(k)$ when $Ro_T = 0.03$. Inset: radial profiles of temporal- and zonal-averaged azimuthal velocity, U_θ. (e) Kinetic energy spectra compensated by k^{-3} and normalized by N^2 versus $L_R k$. The dashed line indicates the plateau segment for $L_R k \in [2, 10]$ with a magnitude of ~0.5. Data for $h = 0.18$ m.

dynamics of terrestrial planets [19]. This model simulated the gradient of solar radiation between the equator and the poles by heating an annular ring on the bottom of the tank at the outer cylinder and cooling a circular plate in contact with the top surface of the fluid at the inner cylinder, which mimics the preferential heating of the ground at low latitudes by the Sun and radiative cooling of the atmosphere from the top at high latitudes, nearer the rotation axis of the planet. The variation of the Coriolis parameter with latitude, i.e., the planetary beta effect, was simulated by a topographic beta effect, in which the system was rotated about its axis of symmetry at a constant angular velocity Ω, and by varying the fluid depth with radius using a conical-shaped plate placed on the bottom; see Fig. 1(a). The annular flow domain had an outer radius $L_o = 0.488$ m and an inner radius $L_i = 0.025$ m. The bottom sloped conically at an angle $\gamma = 15°$ to the horizontal with a volume-averaged fluid depth of $H = 0.236$ m. The fluid at the outermost flat-bottomed annular region was maintained at temperature Θ_o via electrical heating, while the fluid in contact with the top circular plate was maintained at temperature Θ_i via circulation chilling. The inclined bottom was thermally insulated. The free surface exposed the body of fluid to the ambient environment so, in order to minimize the thermal perturbation, the air temperature was maintained at $\Theta_m = (\Theta_i + \Theta_o)/2 \approx 20 \pm 1$ °C. The bottom-heating and top-cooling configurations induced localized free convection in the respective regions above and below, thereby isolating the stably stratified flow in the center of the channel from sidewall boundaries.

The dynamics of baroclinic flows are governed by several key dimensionless parameters. These include the thermal Rossby number $Ro_T = \alpha g H \Delta\Theta / \Omega^2 (L_o - L_i)^2$, the Taylor number $Ta = 4\Omega^2 (L_o - L_i)^5 / H\nu^2$, measuring, respectively, the relative effects of buoyancy and rotation in shaping baroclinic eddies, as well as the Prandtl number, $Pr = \nu/\kappa$. Here, α, ν, κ, g denote the volume thermal expansion coefficient, kinematic viscosity, thermal diffusivity and gravitational acceleration, and $\Delta\Theta = \Theta_o - \Theta_i$. The working fluid was a water-glycerol mixture for which $Pr = 13.3$ for the prescribed Θ_m. Heating power was fixed at 207.6 W, resulting in $\Delta\Theta = 12.2 \pm 0.5$ K as Ω varied from 0.05 to 1.14 rad s^{-1}, covering the range in parameter space $Ro_T \in [0.0279, 14.6]$ and $Ta \in [3.08 \times 10^8, 1.60 \times 10^{11}]$. The average topographic beta effect at a given Ω was quantified by $\bar{\beta} = (2\Omega/H)\{\tan\gamma + [\Delta h/(L_o - L_i)]\}$, where Δh denotes the fluid depth difference between L_o and L_i, accounting for both the conical plate and free surface deformation, $\bar{\beta} \in [0.114, 2.90]$ m^{-1} s^{-1}. Velocity data lasting 1.5 hours were acquired using particle image velocimetry, with measurements beginning one hour after the rotation and heating commenced. The velocity fields were computed via a multistep cross-correlation approach. The resulting radial (meridional) and azimuthal (longitudinal) velocities (u_r, u_θ) in polar coordinates (r, θ), with the origin at the axis of symmetry, had a spatial resolution of 7.5 mm radially and 0.85° azimuthally. Time-averaged energy spectra and interscale transfers at heights $h = 0.12$ and 0.18 m above the flat bottom plate were studied, which are representative of the flow in the predominantly baroclinic region. Comparable results were obtained at two heights, so only results for $h = 0.18$ m are shown in the main text, and results for $h = 0.12$ m are present in the Supplemental Material (SM) [20]. The time-averaged vertical profile of temperature was measured using an array of thermocouples evenly spaced at 3 cm intervals along a rod at $r \approx L_o/2$. A linear fit to the temperature profile between 3 cm above the sloped bottom plate and 18 cm from the flat plane yielded the mean vertical temperature gradient $\langle \Theta_z \rangle_{t,z}$, leading to the Brunt-Väisälä frequency,

$N = \sqrt{\alpha g \langle \Theta_z \rangle_{t,z}}$. Although measured locally, the long-time averaging renders N representative of the baroclinic region due to the azimuthal drift of the waves and the relatively small spatial variation of the temperature gradient in the bulk of the flow [25].

Kinetic energy spectra—Figure 1(b) displays the instantaneous relative vertical vorticity, $\zeta = (1/r)(\partial/\partial r)(ru_\theta) - (1/r)(\partial u_r/\partial\theta)$, at $h = 0.18$ m for $Ro_T = 5.41$. The bulk region is dominated by two eddies edged with fine-scale vorticity filaments. These coherent eddy structures have a radial scale comparable to the Rossby radius of deformation $L_d = NH/(2\Omega)$. As the rotation rate Ω increases in Fig. 1(c), L_d decreases, giving rise to the emergence of smaller wavelength elongated eddies. These eddies evolve with time and propagate in the same direction as the table rotation (see Supplemental Material [20]), resulting in an axisymmetric distribution of the time-averaged kinetic energy. The radial profiles of temporally and zonally (azimuthally) averaged azimuthal velocity, U_θ, in the inset of Fig. 1(d) show the appearance of up to two parallel jet flows. These zonal jets have maximum magnitude $U_\theta^{\max}$ and a width that scales approximately with the Rhines length, $L_R = (2U_\theta^{\max}/\bar{\beta})^{1/2}$.

Figure 1(d) shows the time-averaged horizontal kinetic energy spectrum $E(k) = (1/2dk)\sum_{k_{mn}\in k\pm dk/2}\langle \hat{\mathbf{u}}_{mn}\cdot\hat{\mathbf{u}}^*_{mn}\rangle_t$, where $\langle\rangle_t$ denotes the time averaging, and $\hat{\mathbf{u}}$ and $\hat{\mathbf{u}}^*$ are the complex velocity amplitudes and their conjugates obtained from a Fourier-Bessel transform with basis functions $J_m(k_{mn}r)e^{im\theta}$. Here, J_m is the Bessel function of the first kind and serves as a good approximate basis for an annular domain with a near-central inner boundary, m is the azimuthal mode number, n is the radial index, and k_{mn} is the total (2D) wave number (see SM [20] for more details). The kinetic energy spectrum exhibits a peak at a wave number designated k_p and follows a k^{-3} decay at higher k, characteristic of rotationally dominated flows [14,20]. At higher wave numbers ($k > 100$ m^{-1}), the spectrum transitions to a shallower scaling with an exponent ~ -2.3. With increasing Ω (decreasing Ro_T), k_p shifts to higher values. Additionally, the k^{-3} range expands in wave number and increases in magnitude with smaller Ro_T. This suggests that spectral magnitude increases with Ω but much less steeply than Ω^2 (see SM [20]), in contrast to a recent prediction for rotating turbulence without stratification [26]. Figure 1(e) presents the energy spectra compensated by k^{-3} and normalized by N^2, plotted as a function of kL_R. The resulting curves are seen to collapse toward a quasiuniversal profile and reach a plateau with the magnitude of $c_h \simeq 0.5$ in the range $kL_R \in [2, 100]$. The amplitude c_h is found to be a weak function of height, becoming $\sim$0.3 at the lower height level of $h = 0.12$ m. These results suggest a universal scaling regime in kinetic energy spectra governed by the Rhines length scale L_R and buoyancy frequency N, but with a residual dependence on h. The primary dependence of N^2 was validated by the fact that the magnitude of $E(k)$ decreased proportionally when the heating power was reduced by half [20].

We note that a similar spectrum occurs in forced stably stratified flows, but only with respect to vertical wave numbers in the absence of rotation [26]. Our Letter demonstrates a quantitative connection between the *horizontal* spectral amplitude and vertical stratification, which, to the authors' knowledge, has not explicitly been captured by existing theories. To gain further insight into this relationship, we investigated the spectral fluxes of energy and enstrophy.

Spectral energy and enstrophy flux—We computed the spectral energy flux from the nonlinear energy transfer rate $\tilde{T}_{mnq}$ [27]. This transfer rate represents triad interactions among horizontal flows with azimuthal wave number indices (m, n, q) satisfying $q = m - n$, corresponding to $u_\theta[u_r(\partial u_\theta/\partial r) + (u_\theta/r)(\partial u_\theta/\partial\theta) + (u_\theta u_r/r)] + u_r[u_r(\partial u_r/\partial r) + (u_\theta/r)(\partial u_r/\partial\theta) - (u_\theta^2/r)]$ [28]. In spectral space,

$$\tilde{T}_{mnq} = \hat{u}^*_{\theta,m}\hat{u}_{r,q}\frac{\partial\hat{u}_{\theta,n}}{\partial r} + \frac{in}{r}\hat{u}^*_{\theta,m}\hat{u}_{\theta,q}\hat{u}_{\theta,n} + \frac{1}{r}\hat{u}^*_{\theta,m}\hat{u}_{\theta,q}\hat{u}_{r,n} + \hat{u}^*_{r,m}\hat{u}_{r,q}\frac{\partial\hat{u}_{r,n}}{\partial r} + \frac{in}{r}\hat{u}^*_{r,m}\hat{u}_{\theta,q}\hat{u}_{r,n} - \frac{1}{r}\hat{u}^*_{r,m}\hat{u}_{\theta,q}\hat{u}_{\theta,n}, \tag{1}$$

where $\hat{u}_{\chi,l}(r,t) = \sum_p A_{lp}\hat{\hat{u}}_{\chi,lp}(t)J_l(k_{lp}r)$, the subscript χ denotes the velocity component, and A_{lp} is a normalization coefficient. The effective energy transfer in the baroclinic region, defined as the annular zone between $r_1 = 0.4L_0$ and $r_2 = 0.72L_0$, was also computed as

$$T_{mnq} = \frac{2}{r_2^2 - r_1^2}\int_{r_1}^{r_2}\langle\tilde{T}_{mnq}(r,t)\rangle_t r dr. \tag{2}$$

Figure 2(a) shows T_{mnq} for $Ro_T = 2.10$; energy predominantly transfers locally between adjacent modes, evident in the subdiagonal pattern, corresponding to forward transfer from mode m to $n = m + 3$ (negative T_{mnq}) and into m

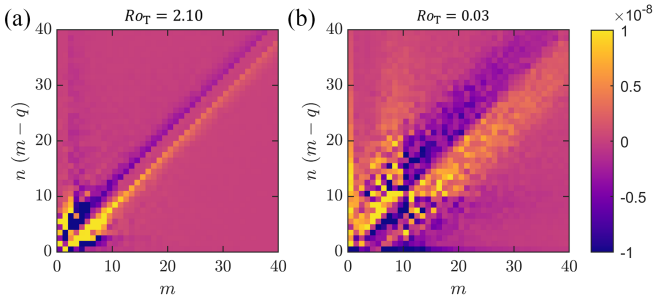

FIG. 2. Energy transfer functions T_{mnq} for triad interactions averaged over the bulk region excluding the convective boundary flows. (a) $Ro_T = 2.10$ and (b) 0.03 for $h = 0.18$ m.

from $n = m - 3$ at the same rate (positive T_{mnq}), reflecting a classical local energy cascade picture. However, for $Ro_T = 0.03$ in Fig. 2(b), forward transfer occurs more nonlocally (off diagonal), while backward (upscale) transfer occurs both nonlocally and locally for certain ranges in m. It is notable that energy transfer to the zonal mode $m = 0$ from various n increases significantly at small Ro_T, indicating an increased role for direct wave-mean flow interaction [4,29].

Figure 3(a) shows the spectral energy flux $\Pi(k)$ computed from the integrals of $\tilde{T}_{mnq}$,

$$\Pi(k) = \frac{2}{r_2^2 - r_1^2} \int_{r_1}^{r_2} \int_{k}^{k_{\max}} \sum_{n} \langle \tilde{T}_{mnq} \rangle_t (r, k', n) dr dk', \quad (3)$$

with $k' = m/r$ and $k_{\max}$ the maximal wave number resolved in our experiments. The flux $\Pi(k)$ quantifies the net energy transfer across wave number k due to nonlinear interactions. For most cases studied, $\Pi(k)$ has a negative peak with a magnitude of Π^p at the low wave number end, crossing zero at $k = k_c$, becoming positive, and eventually approaching zero. The sign change in Π indicates a bidirectional energy transfer: an upscale transfer from small to large scales (i.e., from high to low k) in the range $[k_{\min}, k_c]$, and a downscale transfer in the range $[k_c, k_{\max}]$. The crossover length scale, $L_c := 1/k_c$, representing the smallest length for kinetic energy being transferred effectively upscale, is smaller than, but proportional to, L_d for $Ro_T < 1$, as shown in Fig. 4(a). In contrast, the energy conversion from baroclinic to barotropic modes occurs over a broad range of wave numbers, as found by Larichev [30], substantially broadening the narrow band around L_d suggested by Salmon [1].

The dependence of the spectral amplitude of the k^{-3} scaling on N^2 can be interpreted through the energy conversion processes. Specifically, baroclinic eddies with length scales comparable to or greater than L_d extract available potential energy (APE) stored in an inclined isothermal layer with an angle γ_T to the horizontal plane and convert it into kinetic energy. Assuming approximate

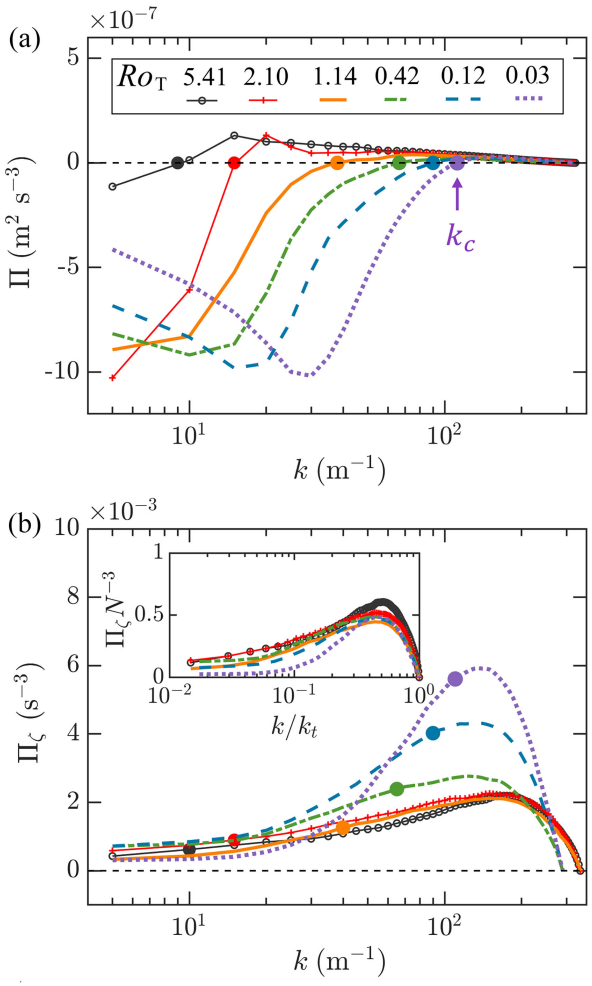

FIG. 3. Spectral fluxes of (a) kinetic energy, Π and (b) enstrophy, Π_ζ, versus k. Inset in (b) indicates the collapse of $\Pi_\zeta N^{-3}$ versus k/k_t, where k_t denotes the wave number that Π_ζ decays to zero. The dots in (a) and (b) indicate the zero-crossing wave numbers k_c of Π. Data for $h = 0.18$ m.

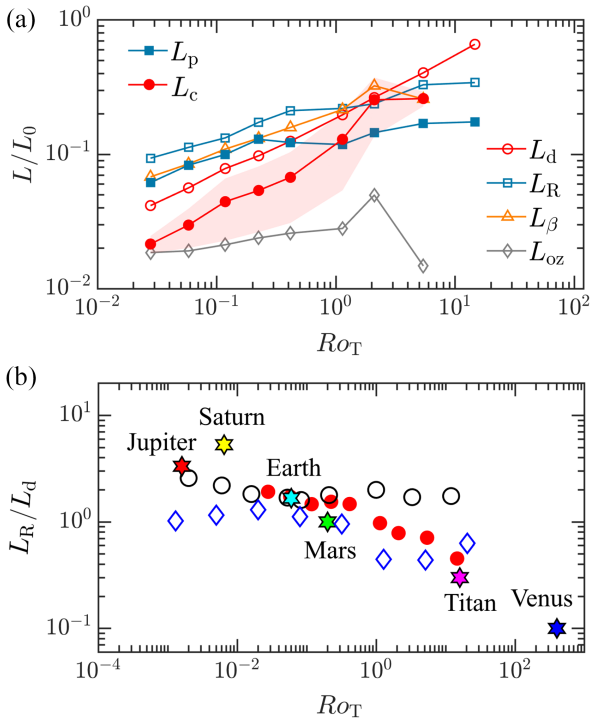

FIG. 4. (a) Characteristic length scales. $L_\beta = (\Pi^p/\bar{\beta}^3)^{1/5}$ and $L_{oz} = (\Pi^p/N^3)^{1/2}$ for length scales at which eddies feel anisotropy associated with Rossby wave propagation and stratification, respectively. The shaded region denotes the uncertainty associated with the determination of L_c. (b) L_R/L_d versus Ro_T for experiments (filled circles, experimental data for $h = 0.18$ m), numerical simulations (empty diamonds from [31] and empty circles from [32]), and planetary atmospheres (stars from [3]).

equipartition between potential and kinetic energy, the eddy velocity scales as $v \sim b'/N$ [8,33], where $(b'/N)^2$ represents the APE per unit mass. We consider buoyancy variations $b' \sim \alpha g \partial T/\partial r(1/k_r)$ across a horizontal length scale $1/k_r$ in a one-dimensional radial system due to the axisymmetry of the flow (the symmetry is restored in the time-averaged flow). The radial temperature gradient can be related to the vertical stratification via $\partial T/\partial r = (\partial T/\partial z)\tan\gamma_{\mathrm{T}}$. Given two components of velocity fluctuations in the same order, they can then be estimated as $v_r \sim v_\theta \sim N/k_r \tan\gamma_{\mathrm{T}} \sim N/k \tan\gamma_{\mathrm{T}}$, assuming $k_r \sim k$. (The total wave number k_{mn} scales with the number of radial zero crossings, and hence, with k_r.) Consequently, $E(k) \sim c_h N^2 k^{-3}$, where c_h is a height-dependent coefficient that accounts for the slope of the isotherms. Assuming $\gamma_{\mathrm{T}} \simeq \gamma$, c_h becomes constant for a given configuration and measurement height, thus revealing a clear N^2 dependence of the k^{-3} part.

The spectral enstrophy flux, Π_ζ, was computed in a way analogous to Π, but using the enstrophy transfer function $\tilde{T}^{\zeta}_{mnq}$:

$$\begin{aligned}\tilde{T}^{\zeta}_{mnq} = &\left(\frac{1}{r}\frac{\partial(r\hat{u}^*_{\theta,m})}{\partial r} + \frac{im\hat{u}^*_{r,m}}{r}\right)\hat{u}_{r,q}\frac{\partial}{\partial r}\left(\frac{1}{r}\frac{\partial(r\hat{u}_{\theta,n})}{\partial r} - \frac{in\hat{u}_{r,n}}{r}\right)\\ &+\frac{in}{r}\left(\frac{1}{r}\frac{\partial(r\hat{u}^*_{\theta,m})}{\partial r} + \frac{im\hat{u}^*_{r,m}}{r}\right)\hat{u}_{\theta,q}\\ &\times\left(\frac{1}{r}\frac{\partial(r\hat{u}_{\theta,n})}{\partial r} - \frac{in\hat{u}_{r,n}}{r}\right). \qquad (4)\end{aligned}$$

The spectral flux of relative enstrophy effectively represents that of potential enstrophy. This is because their differences, arising from the stream function ψ ($\psi \propto (kL_d)^2\zeta$) and the spatial variations in the Coriolis parameter ($\approx 2\Omega - \bar{\beta}r$), have a limited impact on $\tilde{T}^{\zeta}_{mnq}$, particularly in the high-wave-number limit. Π_ζ remains positive throughout the wave number range investigated, as shown in Fig. 3(b), consistent with the forward enstrophy transfer predicted in KLB theory [9]. It is approximately zero for $k < 10\ \mathrm{m}^{-1}$, then increases steeply, reaching a maximum at $k \sim 100\ \mathrm{m}^{-1}$ before declining toward zero. Within Kraichnan's theoretical framework [9], the enstrophy transfer rate, η, at wave number k can be estimated from the energy spectrum as $\eta \sim \int_0^k wp^3 E(p)dp \sim \mathrm{const}$, where the corresponding rate of shear w is represented by $w(k) \sim \int_0^k pE(p)dp$. By substituting the N^2-dependent energy spectrum into the above expressions, we obtain $\eta \propto N^3$. The inset of Fig. 3(b) shows that the large-wave-number parts of $N^{-3}\Pi_\zeta$ seem to collapse onto each other, indicating that $\Pi_\zeta(k)$ exhibits a self-similar shape scaled solely by N and k_{t}. This result supports the consistency between the N^2 dependence of energy spectra and enstrophy-controlled predictions of KLB theory, despite an evident lack of an enstrophy inertial range.

Length scale—Figure 4(a) shows that all the key characteristic length scales have a decreasing trend with decreasing Ro_{T}. The trend of the energy accumulated length, $L_{\mathrm{p}} := 1/k_{\mathrm{p}}$, versus Ro_{T} closely follows that of L_{R}, reflecting the reduction of the characteristic scale in the mean zonal flow with increasing Ω as observed in Fig. 1. L_{R} is smaller than L_{d} for $Ro_{\mathrm{T}} > 2$ and exceeds the latter only when $Ro_{\mathrm{T}} \lesssim 1$. The crossover between L_{R} and L_{d} is associated with changes of energy transfer in Fig. 2 as the energy accumulation in the zonal mean flow increases, leading to $L_{\mathrm{R}}/L_{\mathrm{d}} > 1$. L_{R} and L_{d} are conventionally treated as two independent parameters reflecting the flow properties. However, the ratio $L_{\mathrm{R}}/L_{\mathrm{d}}$ in the inverse transfer regime remains confined to a narrow range of (1, 2) over a wide parameter space within $Ro_{\mathrm{T}} \in [0.01, 1]$, as shown in Fig. 4(b). This result suggests the emergence of a connection between these two scales for weak zonal flows, reminiscent of baroclinic adjustment as indicated for Earth [34]. To interpret this connection, we use the eddy velocity at the deformation radius to estimate the strength of the circulation, i.e., $U_\theta^{\max} \sim NL_{\mathrm{d}}$, yielding $L_{\mathrm{R}} \propto L_{\mathrm{d}}$. The coupling between L_{R} and L_{d} reduces the number of free parameters needed to describe baroclinic systems within the corresponding Ro_{T} regime and offers a means to predict one length scale from the other in planetary atmospheres, as the measurement of L_{d} on planets is not easily available. At smaller Ro_{T}, however, kinetic energy concentrates strongly into zonal jets, potentially leading to a greater value of $L_{\mathrm{R}}/L_{\mathrm{d}}$—a scenario reminiscent of atmospheres on gas giant planets.

In summary, the k^{-3} part of the kinetic energy spectrum in geostrophic turbulence is dictated by the process of enstrophy cascade, but it is also linked with significant bidirectional energy transfer. Both amplitudes of the spectrum and the enstrophy flux are controlled by the degree of stratification. Global numerical weather prediction (NWP) models reproduce the k^{-3} at the Earth's tropopause with the same magnitude even when mesoscale and submesoscale parameterizations are altered. In contrast, the energy transfer across scales and the crossover scale L_c of the spectral flux respond sensitively to these changes, as they depend on how energy is removed at small scales [35]. Diagnostics from reanalyses, constrained by the underlying NWP formulation, thus inherit uncertainties from parameterization biases. Independent experimental observations not reliant on model closures provide essential references to constrain parameterizations, for instance, via comparisons of flux scales such as L_c. For gas giant planets, the energy distribution and transfer associated with the strongly anisotropic zonal jets, determined by the planetary β effect, represent a distinct regime in which eddy dynamics differ. Investigating energy pathways in this anisotropic flow will be a focus of future studies.

Acknowledgments—We acknowledge support from the UK Engineering and Physical Sciences Research Council

(EPSRC) under Grants No. EP/W022087/1 and No. EP/K029428/1. We are grateful to the two reviewers and the editor for their constructive comments.

Data availability—The data that support the findings of this article are openly available [36].

[1] R. Salmon, Geophys. Astrophys. Fluid Dyn. **15**, 167 (1980).
[2] R. M. B. Young and P. L. Read, Nat. Phys. **13**, 1135 (2017).
[3] A. P. Showman, J. Y-K. Cho, and K. Menou, Atmospheric circulation of exoplanets, in *Exoplanets*, edited by S. Seager (University of Arizona Press, Tucson, 2011), pp. 471–516.
[4] *Zonal Jets: Phenomenology, Genesis, and Physics*, edited by B. Galperin and P. L. Read (Cambridge University Press, Cambridge, England, 2019).
[5] H. Khatri, J. Sukhatme, A. Kumar, and M. K. Verma, J. Geophys. Res. Oceans **123**, 3875 (2018).
[6] H. H. Klahr and P. Bodenheimer, Astrophys. J. **582**, 869 (2003).
[7] M. Teitel, D. Schwabe, and A. Y. Gelfgat, J. Cryst. Growth **310**, 1343 (2008).
[8] J. G. Charney, J. Atmos. Sci. **28**, 1087 (1971).
[9] R. H. Kraichnan, Phys. Fluids **10**, 1417 (1967).
[10] G. Boffetta and R. E. Ecke, Annu. Rev. Fluid Mech. **44**, 427 (2012).
[11] G. D. Nastrom, K. S. Gage, and W. H. Jasperson, Nature (London) **310**, 36 (1984).
[12] E. Lindborg, J. Fluid Mech. **388**, 259 (1999).
[13] B. H. Burgess, A. R. Erler, and T. G. Shepherd, J. Atmos. Sci. **70**, 669 (2013).
[14] J. Callies, R. Ferrari, and O. Bühler, Proc. Natl. Acad. Sci. U.S.A. **111**, 17033 (2014).
[15] C. Rodda and U. Harlander, J. Atmos. Sci. **77**, 2793 (2020).
[16] V. Borue, Phys. Rev. Lett. **72**, 1475 (1994).
[17] M. Chertkov, C. Connaughton, I. Kolokolov, and V. Lebedev, Phys. Rev. Lett. **99**, 084501 (2007).
[18] A. M. Rubio, K. Julien, E. Knobloch, and J. B. Weiss, Phys. Rev. Lett. **112**, 144501 (2014).
[19] H. Scolan and P. L. Read, Exp. Fluids **58**, 75 (2017).
[20] See Supplemental Material at http://link.aps.org/supplemental/10.1103/n2nj-dg5r for experimental details, additional analyses, and movies, which includes Refs. [21–24].
[21] W. Thielicke and R. Sonntag, J. Open Res. Software **9**, 12 (2021).
[22] J. Nicholson, Bessel zero solver, MATLAB central file exchange, https://www.mathworks.com/matlabcentral/fileexchange/48403-bessel-zero-solver (2025).
[23] P. L. Read, T. E. Dowling, and G. Schubert, Nature (London) **460**, 608 (2009).
[24] P. L. Read, Planet. Space Sci. **59**, 900 (2011).
[25] C. A. Smith, K. G. Speer, and R. W. Griffiths, J. Phys. Oceanogr. **44**, 2273 (2014).
[26] B. Galperin and S. Sukoriansky, Phys. Rev. Fluids **5**, 063803 (2020).
[27] R. D. Wordsworth, P. L. Read, and Y. H. Yamazaki, Phys. Fluids **20**, 126602 (2008).
[28] L. D. Landau and E. M. Lifshitz, *Fluid Mechanics*, 2nd ed., Course of Theoretical Physics Vol. 6 (Pergamon Press, Oxford, 1987), p. 48.
[29] K. Srinivasan and W. R. Young, J. Atmos. Sci. **69**, 1633 (2012).
[30] V. D. Larichev and I. M. Held, J. Phys. Oceanogr. **25**, 2285 (1995).
[31] Y. Wang, P. L. Read, F. Tabataba-Vakili, and R. M. B. Young. Q. J. R. Meteorol. Soc. **144**, 2537 (2018).
[32] G. P. Williams, Clim. Dyn. **2**, 205 (1988).
[33] G. K. Vallis, *Atmospheric and Oceanic Fluid Dynamics* (Cambridge University Press, Cambridge, England, 2017).
[34] P. Zurita-Gotor and R. S. Lindzen, Theories of baroclinic adjustment and eddy equilibration, in *The Global Circulation of the Atmosphere*, edited by T. Schneider and A. H. Sobel (Princeton University Press, Princeton, NJ, 2007), pp. 22–45.
[35] S. Malardel and N. P. Wedi, J. Geophys. Res. Atmos. **121**, 5395 (2016).
[36] Dataset for this paper: https://ora.ox.ac.uk/objects/uuid:2d287326-32b6-4844-abc2-f9942156d347.